AIAA SciTech Forum
8-12 January 2024, Orlando, FL
AIAA SCITECH 2024 Forum

10.2514/6.2024-0606

Effects of Varying Geometric Design Parameters on the Stability of Deployable Thin-Shell Composite Space Structures

Meital O. Carmi*, Sage Cooley†, and Sergio Pellegrino‡
California Institute of Technology, Pasadena, CA, 91125

Increasing the stability of thin-shell composite structures is important as they become larger and lighter for future applications. This work focuses on varying the cross sectional geometry of thin-shell coilable longerons in an effort to increase both their critical buckling load and stability approaching the buckling load. Stability metrics to quantify the stability of structures with different geometries are defined. 3D-printed and composite longerons with different cross sectional geometries are tested experimentally, and geometrically perfect composite longerons are analyzed numerically. Based on the dominant imperfection that has been observed, the effects of twist on the stability of these structures is investigated.

I. Introduction

Buckling is one of the main failure modes of thin-shell structures. Good characterization of a structure's stability is important because it is desirable to design larger and lighter space structures, which often means designing them to operate closer to their critical buckling load. However, buckling of thin shells is difficult to predict since these structures are very sensitive to imperfections, which can significantly decrease their critical buckling load [1–3] and affect the location where buckling occurs [4]. Composite thin-shell structures, which are increasingly being used in space applications, are anisotropic and often have local defects, making them sensitive to local buckling. Thus, quantifying their buckling behavior and finding ways to increase their stability is crucial, yet especially challenging.

To thoroughly and nondestructively characterize the stability of thin shells, a probing method was previously developed, where a probe locally displaces a structure, to quantify the amount of energy required to trigger early local buckling before the critical buckling load is reached [5, 6]. The probing method has been experimentally applied to characterize the stability of cylindrical shells [6], pressurized elastomeric hemispherical shells [7], and stainless steel tape spring strips [8]. However, the probing technique has never been experimentally used to study thin-shell composite structures, which are particularly prone to local instabilities.

An application of particular interest to this work is the Caltech Space Solar Power Project (SSPP), which aims to generate solar power in space and wirelessly transmit the energy to Earth. The SSPP spacecraft consists of a thin-shell composite structure, which will support a tensioned membrane containing solar cells and RF elements [9]. To simplify the problem, the triangular rollable and collapsible (TRAC) longeron [10], which is a fundamental element of the SSPP structure, will be studied. The TRAC longeron cross section consists of two circular arc flanges connected by a straight web region, as shown in Fig. 1. The web region is always about twice as thick as the flanges.

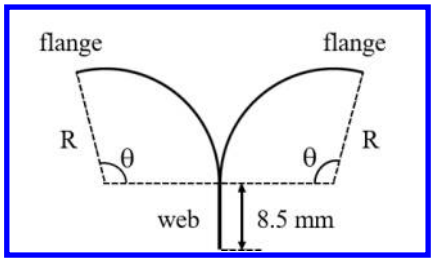

Fig. 1 Longeron cross section where R is the flange radius and θ is the flange subtended angle.

*Graduate Student, Graduate Aerospace Laboratories, 1200 E California Blvd, MC 105-50, AIAA Student Member. mcarmi@caltech.edu
†Wave Fellow at Caltech. Currently Undergraduate Student, Mechanical Engineering Department, Duke University. sage.cooley@duke.edu
‡Joyce and Kent Kresa Professor of Aerospace and Civil Engineering, Graduate Aerospace Laboratories, 1200 E California Blvd, MC 105-50, AIAA Fellow. sergiop@caltech.edu

Though TRAC longerons have been shown to have a stable post-buckling regime, their effective bending stiffness decreases significantly after local buckling occurs [11], which is undesirable for structures required to consistently support a certain load. Thus, this work focuses on varying the geometry of the longeron cross section in order to increase the stability of longerons. The stability of longerons with different geometries will be quantified by loading the longerons in pure bending and probing the flange in compression. The geometric parameters that will be varied are the flange subtended angle, θ, and the flange radius, R, as shown in Fig. 1. Currently, the flange subtended angle is 105°, and local buckling has been observed to occur at the edge of the flanges. Increasing the subtended angle will make the flange edge curve inward and decrease the compressive stress along the edge. Therefore, it is suspected that increasing the flange subtended angle will improve the stability of longerons. Decreasing the flange radius will increase the curvature, potentially increasing stability, while also decreasing the compressive stress along the edge of the flange.

The paper begins by defining the stability metrics that will be used to evaluate the stability of longerons with different cross sectional geometries. To get an idea of the effects of varying the flange subtended angle and radius, the study began by manufacturing and testing 3D-printed longerons in order to iterate over different cross sectional geometries more quickly. Once the 3D-printed results proved promising, the study progressed to experimentally testing composite longerons with different flange subtended angles. Next, a numerical analysis of geometrically perfect composite longerons with different flange subtended angles was performed to compare to the experimental results. To better match the experimental results, a numerical analysis of a twisted composite longeron was also performed. Finally, the experimental and numerical results for composite longerons are compared.

II. Stability Metrics

Two metrics will be used to evaluate the stability of different structures. The first metric is the critical buckling load. Since this paper focuses on structures loaded in bending, the critical buckling load will be defined as the critical bending moment and associated critical rotation at which buckling occurs. This metric is fairly straight forward: structures with a higher critical buckling load are more stable.

In addition to determining the critical buckling load, this work is interested in evaluating the stability of a structure's unbuckled path, or how close a structure is to becoming unstable when it is loaded to a given fraction of its critical buckling load. The energy barrier, defined as the energy input required to cause the structure to transition from its unbuckled state to the unstable, buckled state, has been used in previous publications as a metric to quantify the stability of a structure's unbuckled equilibrium path [5, 6, 8]. To do this, the structure is loaded below its critical buckling load (preload, or imposed displacement or rotation) and probed, measuring the probe force and displacement. If the probe triggers local buckling, the probe force will drop to zero. The energy barrier is determined by computing the area under the probe force vs. displacement curve up to the point where buckling occurs (probe force equals zero) as shown in Fig. 2a. To study a structure's stability at multiple points along its unbuckled path, the energy barrier has been plotted vs. preload or imposed rotation, for a given probe location on the structure [6, 8].

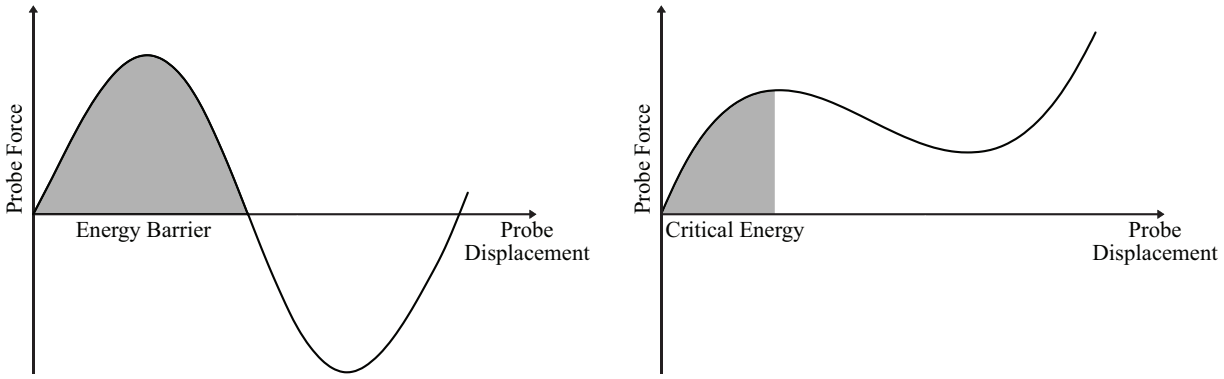

(a) Energy barrier **(b) Critical energy**

Fig. 2 The energy barrier between pre-buckled and post-buckled states [8], left, is the area under the probe force vs. displacement curve up to buckling, while the critical energy, right, is the area under the curve up to the local maximum.

The issue with this previously used metric is that the energy barrier can only be computed if local buckling occurs. However, the probe does not always trigger local buckling. For TRAC longerons, it is much more common to see experimental probe force vs. displacement results similar to Fig. 2b where a local maximum occurs, yet buckling is not triggered. Thus, an alternative metric, the energy to the local maximum of the probe force vs. displacement curve, is defined in this work and will be referred to as the "critical energy". This is the energy input required to trigger an initial instability in the structure, since the structure first becomes unstable when the probe force begins decreasing after reaching the local maximum. The critical energy is calculated by integrating the probe force vs. displacement curve up to the local probe force maximum, as shown in Fig. 2b. This is a more robust metric than the energy barrier since the critical energy can be computed whenever a local maximum in the probe force vs. displacement curve occurs without requiring buckling to be triggered.

Similar to the energy barrier, the critical energy can be computed at several increasing preloads (or imposed rotations) approaching the critical buckling load and plotted vs. preload (imposed rotation). (In this work, a rotation is applied to bend a structure, so the terminology of imposed rotation will be used.) This is particularly useful for evaluating structures with different geometries, since they have different critical buckling loads, and thus a different range of imposed rotations where a local maximum occurs, making it unclear at which single rotation to compare the critical energy. Comparing the trends of critical energy vs. imposed rotation for different structures gives a quantitative comparison of the structures' stability as they approach their buckling loads: structures with a higher critical energy at all imposed rotations are more stable. The critical energy at the critical buckling load is defined to be zero because at the critical bucking load instability occurs before any probe force is applied, so there is zero area under the probe force-displacement curve.

The energy barrier decreases with increasing imposed load and approaches zero as the load approaches the critical buckling load [6]. It was desired to verify that the critical energy would behave similarly, so a numerical model of a longeron was created and the trends of both the energy barrier and critical energy with increasing imposed rotation were computed. A numerical analysis had to be performed for this comparison, rather than experimental tests, since the probe can consistently trigger local buckling (allowing for calculation of the energy barrier) numerically, though it does not experimentally. The shapes of the trends were found to be nearly identical for both the energy barrier and the critical energy. The main difference is that the magnitude of the critical energy is about half the magnitude of the energy barrier, as expected, since the critical energy integrates over about half the area as the energy barrier. Thus, the critical energy behaves similarly to the energy barrier when both can be computed, yet it can be calculated in many cases when the energy barrier cannot be computed. For this reason, the trend of the critical energy as the imposed rotation increases will be used as the second metric to quantify stability throughout the rest of this paper.

III. Experimental Methods

To study the stability of TRAC longerons, a test sample is loaded in pure bending and the buckling behavior of the side in compression is investigated. To perform a probing experiment, a rotation is applied to bend the longeron (imposed rotation), loading one side in compression and one side in tension. Then, a local displacement (probe) is applied to a point on the edge of the longeron in compression. In the current study, the probe is perpendicular to the longeron edge and acts in the direction that will flatten the flange. The probe force vs. displacement is measured in order to determine the critical energy. For less stable structures, the probe force, and thus critical energy, will be fairly low for all imposed rotations, while for more stable structures, the probe force and critical energy will be higher.

A. Experimental Setup

The TRAC longeron is very sensitive to loading and boundary conditions so it is important to apply a well characterized load and minimize the effects of all other loads. This is achieved by using a specifically designed bending machine, which uses air bearings, sliders and counterweights to ensure that there is no redundancy in the boundary conditions, while a motor rotates one end of a sample to apply as close as possible to pure bending about the vertical axis [8]. Load cells on each end of the test structure measure forces and moments in all three directions, to determine the bending moment about the vertical axis as the sample is rotated and verify that all of the other forces and moments are negligibly small. A CAD model of the bending machine and the boundary conditions at the two ends of the sample are shown in Fig. 3a.

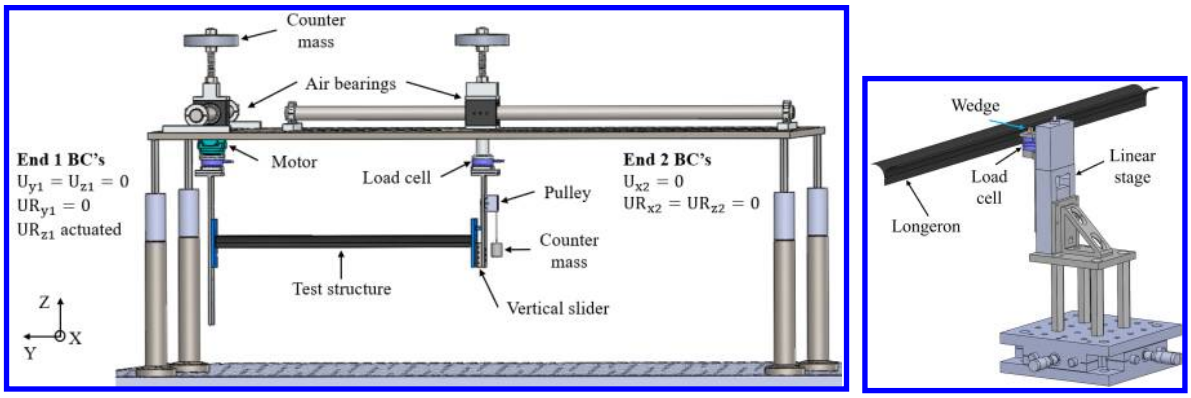

(a) (b)

Fig. 3 (a): CAD model of the bending machine and its boundary conditions. (b): Probing apparatus shown with the wedge positioned on the edge of the longeron.

Once the strip is bent, a probing apparatus, which consists of a small Teflon wedge attached to a load cell that is mounted on a linear translation stage [8], is used to apply a displacement to a point on the edge of the longeron in compression. The load cell measures the probe force, while an incremental encoder on the linear stage measures the probe displacement. A CAD model of the probing apparatus is shown in Fig. 3b.

B. Experimental Procedure

Each test sample consisted of a longeron bonded to acrylic end plates. The acrylic plates were attached to the aluminum plates on either side of the bending machine (End 1 and End 2 in Fig. 3a). A counter mass equalling half the mass of the sample was attached through a low-friction pulley to allow the vertical slider to move freely. All sensors were zeroed before mounting the sample to the bending machine. After mounting the longeron, the moment about the vertical axis was brought to zero via angular displacement of the actuated end (End 1).

Once all forces and moments were set to zero, the longeron was incrementally rotated about the vertical axis. The rotation applied to the longeron was increased until a visible buckle had formed. After finding the approximate critical buckling rotation in this way, the sample was rotated 0.1° to 0.2° past it, measuring the bending moment vs. rotation, to determine the exact buckling load. The exact critical buckling load is indicated by a drop in the bending moment or decrease in the slope of the moment-rotation curve. The slope of the bending moment vs. rotation curve prior to buckling is the bending stiffness of the longeron.

After the critical bending moment and critical rotation had been measured, the longeron was rotated to a value below the critical buckling rotation and probed. The probe was positioned on the edge of the longeron flange under compression and slowly raised as the probe force vs. probe displacement data was collected. In this study, all samples were probed in the center, unless otherwise indicated, as the center was found to generally be the weakest point lengthwise on the longeron. Multiple trials were conducted for different imposed rotations. The imposed rotation was typically far from the actual buckling rotation of the longeron when the probe force vs. displacement relationship increased monotonically for 2-3 millimeters of displacement. For imposed rotations closer to the buckling load, however, a local maximum followed by a local minimum could be observed before the samples re-stabilized. The occurrence of a local maximum allowed for the critical energy to be computed at that imposed rotation. Occasionally, a local buckle could be triggered while probing, generating a local maximum preceding a local minimum where the probe force dropped to zero in the corresponding probe force vs. displacement curve. In this case, the local maximum corresponds to the vertical probe force required to trigger buckling, while the local minimum is the point at which the buckle forms.

C. 3D-Printed Longerons

Longerons with various cross sectional geometries were 3D-printed using generic PLA on a Bambu Lab X1 Carbon FDM (fused deposition modeling) 3D-printer in the vertical orientation (normal to the build plate). The vertical orientation was chosen because it keeps every cross section normal to the nozzle and build plate exactly the same and avoids the support material required in the horizontal case. However, this orientation limited the length of the longerons to less than the printer's vertical build height of 250 mm. All samples were 245 mm long, and had a 400 µm thick web

region and 200 µm thick flanges. The flange thickness was limited by the 200-micron nozzle diameter, which is the smallest nozzle size that the BambuLab X1 Carbon could accommodate. Though this is about twice the thickness of the composite longerons currently used for SSPP structures, the PLA longerons still exhibited buckling instabilities, as will be discussed in the next section.

The ends of the longerons were glued into 6 mm thick acrylic plates with grooves matching the longeron cross section that left enough space for epoxy. The end plates were then mounted onto the bending machine to perform bending and probing tests. The rigid connection of the longeron to the end plates allows the bending machine boundary conditions to be applied directly to the longeron. An example of a 3D-printed longeron glued into the end plates is shown in Fig. 4a.

Longerons with four different cross sectional geometries were tested. The geometry that is currently used in SSPP structures, which has a flange subtended angle of 105° and flange radius of 13.6 mm, was used as the control case. Then, the flange subtended angle was increased to 120° and 135° for two respective samples, while keeping the flange radius at 13.6 mm. Finally, the flange radius was decreased to 11 mm for one sample, while keeping the flange subtended angle at 105°.

D. Composite Longerons

As will be discussed in the next section, experiments with 3D-printed longerons with various flange subtended angles showed that increasing the subtended angle could improve their stability. Thus, the next set of experiments studied composite longerons. All of the composite samples were 500 mm long. The flanges were 100 µm thick and had a layup of $[\pm 45_{GFPW}/0_{CFUD}/\pm 45_{GFPW}]$. The web region was 200 µm thick and had a layup of $[\pm 45_{GFPW}/0_{CFUD}/\pm 45_{3,GFPW}/0_{CFUD}/\pm 45_{GFPW}]$. Here CFUD represents a unidirectional Pyrofil MR 70 12P carbon fiber ply manufactured by Mitsubishi Chemical that is 30 µm thick, and GFPW represents a plain weave scrim glass ply that is 25 µm thick. Both the carbon fiber and scrim glass plies were impregnated with North Thin Ply Technology's ThinPreg 415 resin. The composite longerons were manufactured in the lab using the methods described in [11]. The ends of the longerons were rigidly glued into acrylic plates that mount onto the bending machine, using the same procedure as for the 3D-printed longerons. An example of a composite longeron is shown in Fig. 4b.

Longerons with three different flange subtended angles were tested, all with a flange radius of 13.6 mm. As with the 3D-printed samples, a longeron with 105° flange subtended angle was used as the control case. Then, the subtended angle was increased to 120° and 135° for two respective samples. For uniformity, all three longerons were manufactured from one long longeron, which was cut into three 500 mm long longerons after curing. Then, the flanges of each longeron were cut to the respective subtended angle.

(a) **(b)**

Fig. 4 3D-printed longeron test sample, (a), and composite longeron test sample, (b), glued into acrylic plates.

IV. Experimental Results

A. 3D-Printed Longeron Results

The bending moment vs. rotation angle was measured for each of the 3D-printed longerons. The results are plotted in Fig. 5 below. Each curve ends at the highest rotation that was applied to the respective sample. A sharp drop in the bending moment, as seen near the end of each of the curves, indicates that the critical buckling load has been reached and a buckle has formed somewhere along the length of the flange in compression. All observed buckles formed on the very edge of the flange and were in an upwards direction, i.e., corresponding to flattening the flange.

The bending moment vs. rotation curves for all of the samples are linear up to the critical buckling load, as expected since PLA is a linear elastic material. As mentioned in Section III, the slope of the bending moment vs. rotation curve is the bending stiffness of the respective longeron. Two control samples with 105° flange subtended angle were tested to

verify the repeatability of the 3D-printed longerons. The bending stiffness as well as the critical buckling moment and rotation are about the same for both of the control samples, as shown in Table 1. Therefore, only one sample was tested for each of the other geometries, and the results for only one of the control samples are shown in Fig. 5.

The bending stiffness increases with increasing flange subtended angle, with the 135° flange subtended angle being the stiffest. The longeron with the smaller 11 mm radius flange was the most compliant. This is expected because the smaller flange radius means that the edge of the flange is closer to the neutral axis, so the bending stiffness is lower. The critical buckling bending moment increases with increasing flange subtended angle, though the critical buckling rotation remains about the same, as seen in Table 1. This makes sense given the increasing stiffness as the subtended angle increases. The longeron with a smaller radius flange has about the same critical bending moment as the control longerons, though its critical rotation is significantly higher. This suggests that the critical bending moment is governed by the flange subtended angle irrespective of the flange radius. Since the smaller radius longeron is more compliant, a larger rotation was required to achieve the same critical bending moment.

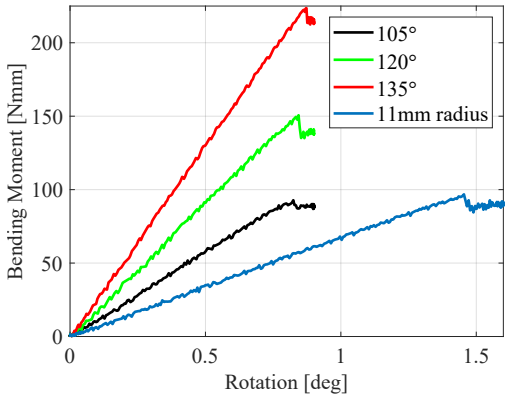

Fig. 5 Bending moment vs. rotation angle for all 3D-printed geometries tested. The sharp drop in bending moment near the end of each curve indicates the critical buckling load.

Table 1 Critical Buckling Bending Moments and Rotations for All 3D-printed Geometries Tested

Flange Geometry	Crit. Bending Moment (Nmm)	Crit. Rotation (deg)
105° (sample 1)	96.5	0.846°
105° (sample 2)	92.8	0.824°
120°	151	0.844°
135°	223	0.873°
11mm radius	96.8	1.46°

Probing tests were conducted for one of the 105° flange subtended angle control longerons, and the 135° flange subtended angle and 11 mm flange radius longerons. The probe force vs. displacement curves at increasing imposed rotations, for the 105° and 135° flange subtended angles, are shown in Fig. 6. The curves for the 11 mm flange radius look similar to those of the control sample so they are not shown. For the control 105° flange, there were only three rotations where a local maximum in the probe force vs. displacement curve was observed, and thus the critical energy could be computed, before the critical buckling load was reached. On the other hand, for the 135° flange longeron, a local maximum occurred for six different rotation values before reaching the critical buckling load (four of these curves are shown in Fig. 6b).

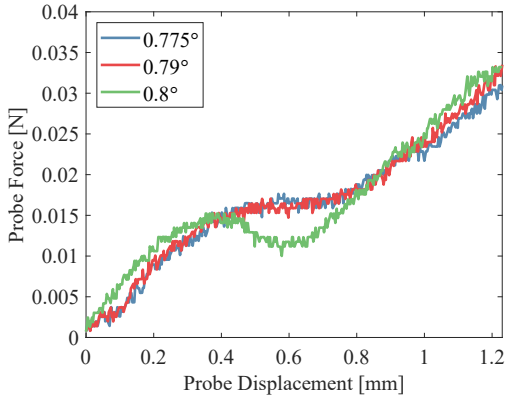

(a) Probe F vs. U for θ = 105°, various rotations

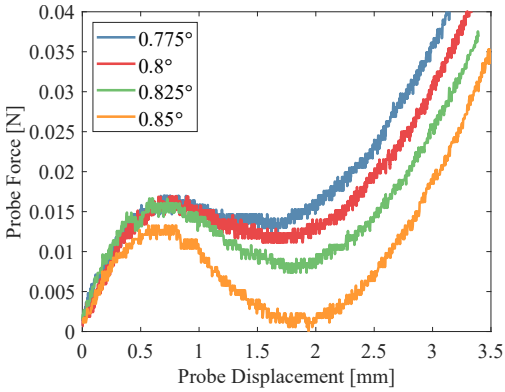

(b) Probe F vs. U for θ = 135°, various rotations

Fig. 6 Probe force vs. displacement curves at various imposed rotations for 3D-printed longerons with θ = 105° and θ = 135°.

The critical energy of the probe force vs. displacement curves at increasing imposed rotations was computed for each of the three samples tested. The resulting energy trends are plotted in Fig. 7 as a function of the fraction of the critical buckling rotation $\left(\frac{\alpha}{\alpha_{cr}}\right)$ of each sample. The energy at the critical buckling load, $\frac{\alpha}{\alpha_{cr}} = 1$, is set to zero for all samples by definition. The fraction of the critical rotation is used rather than the absolute rotation, to more easily compare the stability of each of the geometries near their critical buckling load despite the differing values of their critical moments and rotations. As seen in Fig. 7, the 135° subtended angle has a significantly higher critical energy than the control at all $\frac{\alpha}{\alpha_{cr}}$. The critical energy of the 11 mm radius sample is about the same as that of the control. This suggests that increasing the flange subtended angle increases the stability of the longerons near their critical buckling load, while also increasing the critical buckling load itself. On the other hand, decreasing the flange radius does not have much effect on the stability near the critical buckling load or the value of the buckling load itself. These promising results prompted further study of increased flange subtended angles in composite longerons.

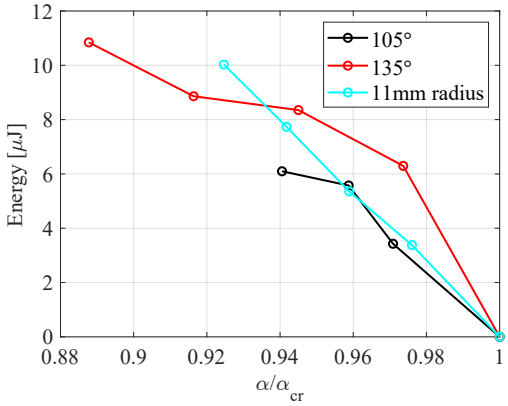

Fig. 7 Comparison of critical energy vs. fraction of the critical buckling rotation for 3D-printed longerons.

B. Composite Longeron Results

One composite longeron with each flange subtended angle, 105°, 120° and 135°, was tested. All three composite longerons had a visible twist. This defect was likely introduced during the manufacturing process and occurs in all three composite longerons since they were manufactured out of the same longer longeron. The twist is zero at the ends of the longeron test samples since they are glued straight in the acrylic end plates, and is most significant at the center of the longerons. This results in one flange bowing downward in a saddle shape, while the other bows upward. All three samples were bent such that the flange bowing downward was in compression. For the control sample with 105° flange subtended angle, the twist was measured to be about 5° at the center of the longeron.

The bending moment vs. rotation angle was measured as each of the composite longerons were loaded in bending and is shown in Fig. 8. Similar to the 3D-printed longerons, each curve shows the highest rotation applied to the respective longeron. The location of the critical buckling load for the composite longerons is indicated by a decrease in the slope of the bending moment vs. rotation curve occurring at the same time as a visible buckle forming on the edge of the flange in compression. Since there is no sharp decrease in bending moment at the critical buckling load and the decrease in slope is fairly subtle, the formation of a visible buckle had to be used as a further indication of having reached the critical buckling load. All observed buckles occurred on the very edge of the flange and formed upwards in the direction that flattens the flange, similar to the 3D-printed samples. The critical bending moments and rotations for all three composite longerons are listed in Table 2. When looking carefully at Fig. 8, a decrease in the slope can be seen at these rotations for the respective samples, as indicated by the circles in the figure.

The moment vs. rotation curve is linear up to the critical buckling load for all of the composite samples, as expected. The bending stiffness increases with increasing flange subtended angle, following the same trend seen for the 3D-printed longerons. The critical bending moment increases with increasing flange subtended angle, though the critical rotation remains about the same, which is expected given the increasing stiffness. These results suggest that increasing the flange subtended angle increases the stability of the longerons. In most applications, structures are loaded with a bending moment, rather than a rotation, so increasing flange subtended angle would allow structures to support a greater moment, with about the same angular deflection, without buckling.

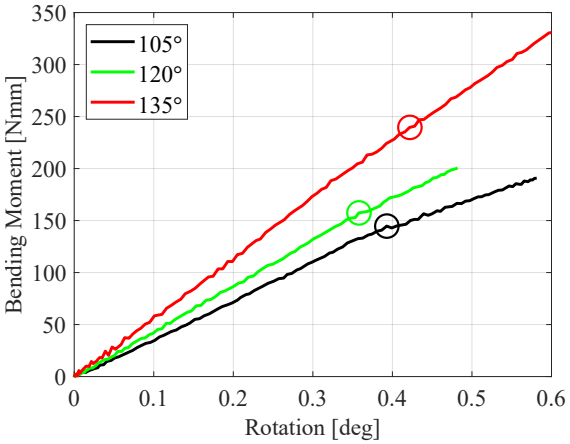

Fig. 8 Bending moment vs. rotation angle for composite longerons with different flange subtended angles. The circles highlight a decrease in the slope of each curve which indicates buckling.

Table 2 Critical Buckling Bending Moments and Rotations for All Composite Structures Tested

Flange Geometry	Crit. Bending Moment (Nmm)	Crit. Rotation (deg)
105°	143	0.39°
120°	161	0.365°
135°	238	0.42°

Probing tests were conducted on the composite longerons with 105° and 120° flange subtended angles. The probe force vs. displacement curves for the longeron with 105° flange subtended angle, at increasing imposed rotations, are shown in Fig. 9. As the imposed rotation increases (from the red curve to the pink curve) and the sample gets closer to its critical buckling load, the probe force at a given displacement decreases. For the smaller rotations of 0.2° and 0.3°, the probe force increases monotonically. A local maximum in the probe force first appears at a rotation of 0.35°. Since the occurrence of a local maximum is required in order to compute the critical energy, it is only computed for imposed rotations of 0.35° or greater. As the rotation continues to increase, the value of the local maximum decreases and it occurs at lower probe displacements, until the critical buckling load is reached. The probe force vs. displacement curves for the 120° subtended angle longeron are similar, and hence, are not shown. A local probe force maximum first

occurred at a rotation of 0.34° for the 120° subtended angle longeron, so the critical energy could only be computed for rotations of 0.34° or greater.

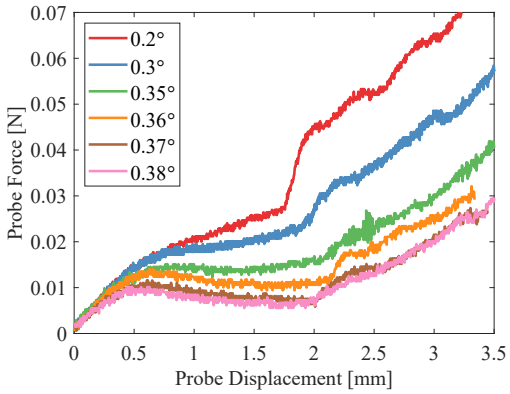

Fig. 9 Probe force vs. displacement curves at various imposed rotations for composite longeron with $\theta = 105°$.

The critical energy at increasing imposed rotations was computed for both the 105° and 120° subtended angle composite longerons, as shown in Fig. 10. The energy at the critical buckling rotation for each sample is set to zero by definition. From the probe force vs. displacement curves in Fig. 9, it is easy to see how the area under the curve (energy) up to the local maximum decreases with increasing imposed rotation. The critical energy for the 120° flange subtended angle sample is much higher than for the 105° sample. As discussed in Section II, the critical energy is used to quantify stability. Therefore, this suggests that increasing the flange subtended angle significantly increases the stability of composite longerons near their critical buckling load.

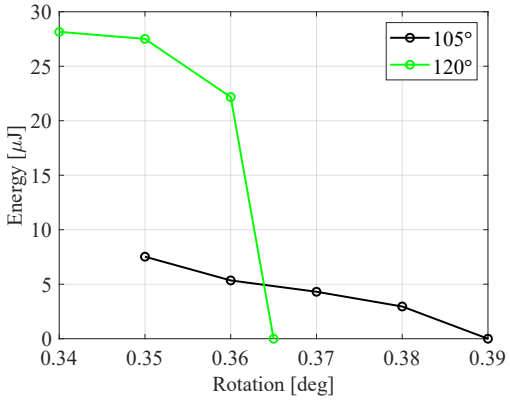

Fig. 10 Comparison of critical energy trend with increasing imposed rotation for experimental composite longerons with $\theta = 105°$ and $\theta = 120°$.

V. Numerical Analysis and Results

A. Numerical Model

To compare the experimental results to the behavior of a perfect longeron, a numerical model of the composite longeron on the bending machine was created using the ABAQUS finite element software. The modeled longerons have the same geometry as the experimental test samples. Tensile and bending tests were conducted on the composite web and flange materials to determine the material properties to use in the simulation. Great care was taken to model the compliance of the bending machine so that the overall bending stiffness of the numerical model would agree with that of the experimental results. The bending machine boundary conditions shown in Fig. 3a are applied to the longeron, with a rotational boundary condition applied to the left end to load the structure in pure bending.

The experimental testing procedure is modeled as closely as possible. First the longeron is rotated to just below the critical buckling load, saving the bending moment vs. rotation angle data. Then, an eigenvalue analysis is performed to compute the critical buckling load. Next, the longeron is bent to a rotation lower than critical value and probing is simulated by applying a displacement boundary condition to a point on the edge of the longeron in compression and measuring the resulting probe force at that point.

B. Numerical Results for Perfect Longerons

A perfect composite longeron with each flange subtended angle, 105°, 120° and 135°, was modeled. The bending moment vs. rotation angle was measured for each of the three modeled longerons and is plotted in Fig. 11. Each curve shows the highest rotation applied to the respective longeron before numerical convergence issues were encountered approaching the critical buckling load. The decrease in the slope of the bending moment vs. rotation curve seen experimentally at the critical buckling load cannot be obtained numerically due to convergence issues. However, the critical buckling rotation and associated critical bending moment can be computed using an eigenvalue analysis.

The bending moment vs. rotation curve is linear for the perfect longerons with all three flange subtended angles, agreeing with the experimental results. The bending stiffness increases with increasing flange subtended angle, also agreeing with the experimental results. The trend of increasing critical bending moment with increasing flange subtended angle is also seen for the perfect longerons, as shown in Table 3. However, the value of the critical bending moment for each of the numerical perfect longerons is significantly higher than that of the corresponding experimental composite longeron. Also, the critical rotation for the perfect longerons increases with increasing flange subtended angle, while it remains about the same for the experimental composite longerons. These discrepancies between the experimental and numerical results is likely due to the twist and other potential defects in the experimental longerons decreasing their critical buckling load.

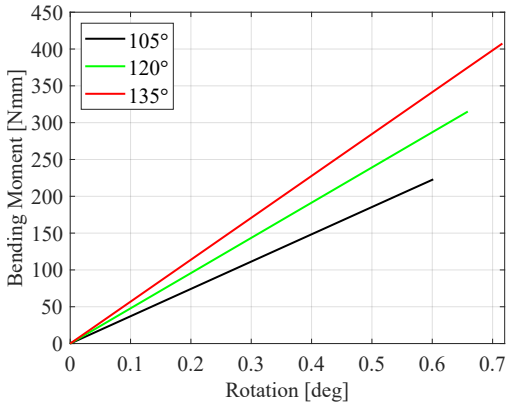

Fig. 11 Bending moment vs. rotation angle for perfect longerons with varying flange subtended angle. Each curve ends at the critical buckling load for the respective longeron where the solver could no longer converge.

Table 3 Critical Buckling Bending Moments and Rotations for Numerical Perfect Longerons

Flange Geometry	Crit. Bending Moment (Nmm)	Crit. Rotation (deg)
105°	223.45	0.603°
120°	316.86	0.663°
135°	407.52	0.716°

The numerical probe force vs. displacement curves at increasing imposed rotations for the perfect longeron with 105° flange subtended angle are shown in Fig. 12. For the numerically simulated longerons, a local maximum in the probe force occurs starting at an imposed rotation of about 60% of the critical buckling load (0.361° for the 105° longeron). At rotations of about 65% of the critical buckling load (0.392° for the 105° longeron) and greater, the probe triggers local buckling and the probe force decreases to zero and becomes negative until the longeron regains stability.

Numerical convergence is difficult once instability occurs making it challenging to resolve the probe force-displacement curve much beyond the point of instability, especially for higher imposed rotations. As the rotation increases, the local probe force maximum clearly decreases in magnitude and occurs at a lower probe displacement, as seen in Fig. 12. The probe force vs. displacement curves for the 120° and 135° subtended angle longerons look very similar to the ones for the 105° longeron so they are not shown.

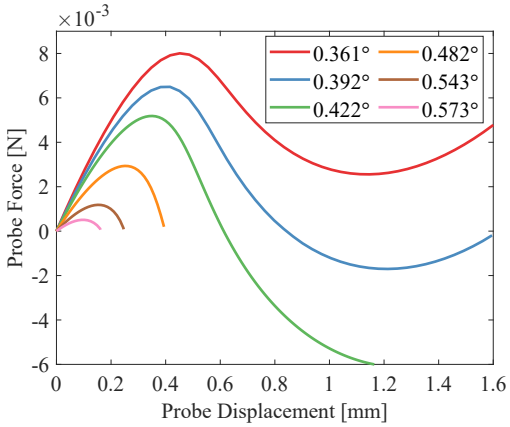

Fig. 12 Numerical probe force vs. displacement curves at various imposed rotations for the perfect longeron with $\theta = 105°$. For rotations of 0.422° and greater, the curves end when numerical convergence is no longer achieved.

The critical energy vs. imposed rotation is plotted for the perfect longerons with all three flange subtended angles in Fig. 13. As with the experimental results, the energy at the critical buckling rotation for each flange subtended angle is set to zero. The critical energy at all imposed rotations increases with increasing flange subtended angle, with the energy for the 135° subtended angle longeron being the greatest. This agrees with the trend seen for both the experimental 3D-printed and composite longerons. However, the magnitude of the critical energy for the numerically simulated longerons is much smaller than that of the experimental composite samples. Additionally, the shape of numerical critical energy vs. imposed rotation curves is quite different from the shape of the experimental curves. The numerical curves exponentially decay to zero energy at the critical buckling load, while the experimental curves have a more linear shape with the energy remaining fairly large up to the critical buckling load.

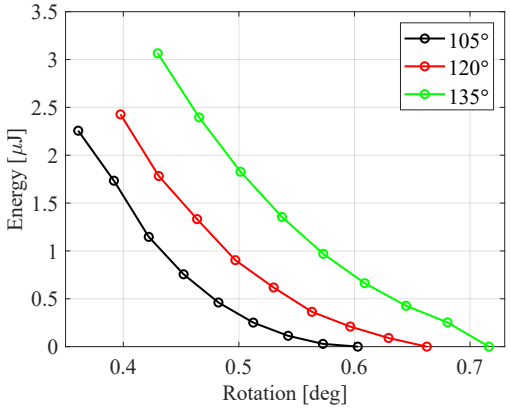

Fig. 13 Comparison of numerical critical energy for increasing flange subtended angle.

C. Numerical Analysis of Twisted Longeron

The main defect in the experimental composite longerons is that they are twisted, so it was suspected that the twist may be causing the discrepancies between the experimental and numerical results. To check this hypothesis, a twisted

longeron was analyzed numerically. A longeron with 105° flange subtended angle was modeled with a twist that linearly increases from zero at the ends to 5° in the center. The longeron was bent such that the flange bowing downwards due to the twist was loaded in compression, as in the experimental tests. The critical buckling bending moment for the twisted longeron is 186.3 Nmm, which is still higher than that of the experimental composite longeron but much closer than the perfect longeron (see Table 4 for a comparison of buckling loads). The probe force vs. displacement curves at increasing imposed rotations for the twisted longeron are shown in Fig. 14a. In contrast to the curves for the perfect longeron, the magnitude of the local probe force maximum decreases only slightly with increasing rotation and occurs at about the same probe displacement. Also, the probe does not trigger local buckling even at rotations very close to the critical buckling rotation.

The trend of the critical energy with increasing imposed rotation for the twisted longeron is shown in Fig. 14b. In contrast to the trend for the perfect longeron, the critical energy trend for the twisted longeron decreases only slightly with increasing imposed rotation, does not decrease monotonically, and remains large up to right before the critical buckling rotation. When looking at the probe force-displacement curves in Fig. 14a, it makes sense that the critical energy would decrease only very slightly since the area under the curves up to the local maximum is about the same for all rotations. A potential explanation of why the twist causes such different stability behavior will be discussed in the next section.

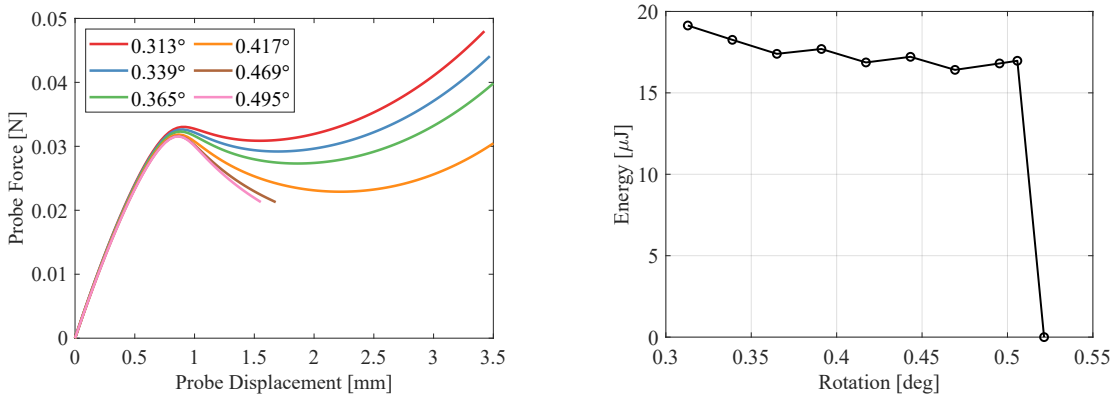

(a) **(b)**

Fig. 14 (a): Numerical probe force vs. displacement curves at increasing rotations for the twisted longeron. For reference, the critical buckling rotation is 0.521°. (b): Critical energy vs. rotation trend for twisted longeron.

VI. Comparison of Experimental and Numerical Results

Insights can be gained as to why the experimental results for the composite longerons differ so significantly from the numerical ones by comparing the experimental results to the results of the numerical perfect and twisted longerons, all with a 105° flange subtended angle. The twisted longeron's critical buckling bending moment and rotation are significantly lower than those of the perfect longeron and closer to those of the experimental longeron, as shown in Table 4. This suggests that the twist is one reason that the experimental critical buckling moment and rotation are so much lower than those for the numerically simulated perfect longeron. More broadly, this indicates that twist, like most other imperfections, decreases a longeron's critical buckling load.

Table 4 Comparison of Critical Buckling Bending Moments and Rotations for Experimental, and Numerical Perfect and Twisted Longerons with $\theta = 105°$.

	Crit. Bending Moment (Nmm)	Crit. Rotation (deg)
Experimental	143	0.39°
Numerical Perfect	223.45	0.603°
Numerical Twisted	186.3	0.521°

The probe force vs. displacement curves for the experimental, numerical perfect and numerical twisted longerons all with 105° flange subtended angle are compared in Fig. 15. The magnitude of the probe force maximum for the numerical perfect longeron is significantly lower than that of the experimental longeron and the numerical twisted longeron. The curves for the experimental and numerical twisted longerons are similar in that the magnitude and location of the local maximum remains about the same as the imposed rotation increases, though this phenomenon is more pronounced for the numerical twisted longeron. In contrast, the curves for the numerical perfect longeron have a decreasing local maximum that occurs at smaller probe displacements as the rotation increases.

The different behaviors of the probe force-displacement curves result in significantly different critical energy trends for the experimental, numerical perfect and numerical twisted longerons, as shown in Fig. 16. The critical energy for the numerical twisted longeron is an order of magnitude greater than for the perfect and the experimental longerons. However, the shape of the trend for the numerical twisted longeron is similar to that of the experimental longeron in that they both remain large up to the buckling load. For both the probe force-displacement curves and the critical energy trend, the experimental results are in between the results for the numerical perfect and twisted longerons, and not too similar to either. The difference between the experimental and numerical twisted results could be because the assumption that the twist increases linearly from the ends to the center of the longeron is not realistic, or because the experimental longeron has additional defects that affect its behavior. The experimental results falling between the results for numerical perfect and twisted longerons suggests that twist is likely what causes the experimental results to differ from the numerical perfect results, and that the numerical model of the twisted longeron needs to be modified to better match the experimental results. Comparing the critical energy trend of the numerical twisted longeron to that of the perfect longeron suggests that the twist increases the stability of longerons as they approach their critical buckling load.

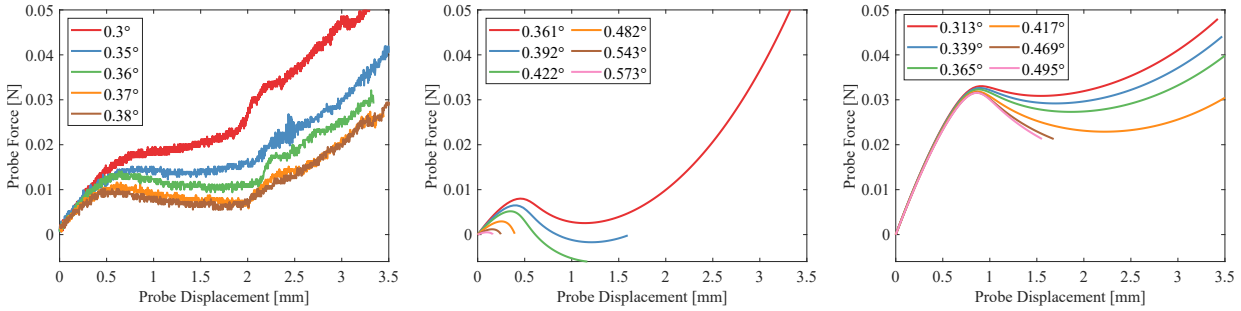

(a) Experimental composite longeron **(b) Numerical perfect longeron** **(c) Numerical twisted longeron**

Fig. 15 Comparison of probe force vs. displacement curves for experimental, and numerical perfect and twisted longerons with $\theta = 105°$.

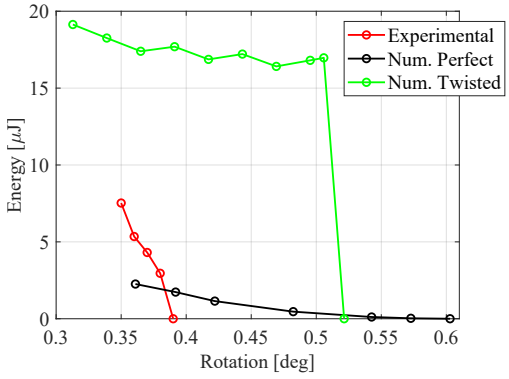

Fig. 16 Comparison of critical energy vs. rotation trend for experimental, and numerical perfect and twisted longerons with $\theta = 105°$.

In order to determine what specifically about the twist causes the different behavior of the probe force-displacement curves, the probe force was plotted as a function of the vertical displacement of the flange at the probe location, measured

from the initial unloaded state, for both the numerical perfect and twisted longerons, as shown in Fig. 17a and 17b. In the typical probe force vs. probe displacement curves, the probe displacement begins at zero, by definition, and any displacement of the flange due the imposed rotation is not accounted for. Plotting the probe force vs. flange displacement clearly shows the effects of the bending, since the displacement at the beginning of the curves (where the probe first makes contact with the flange) is the displacement of the flange due to the imposed rotation. As seen in Fig. 17a, for the perfect longeron the initial flange displacement increases very slightly with increasing rotation and is in the upwards direction. It makes intuitive sense that as the imposed rotation increases the edge of the flange moves up slightly, since it is approaching the formation of an upwards buckle. However, for the twisted longeron, the edge of the flange has a saddle shape due to the twist. This causes the flange to move downward quite significantly with increasing rotation, as shown in Fig. 17b.

To more clearly see this behavior, the vertical displacement of the edge of the flange in the center of the longeron (probe location) is plotted as a function of rotation during the bending step for both the perfect and twisted longerons, as shown in Fig. 17c. The downward flange displacement for the twisted longeron means that a greater probe displacement is required before a local probe force maximum occurs, which explains why the critical energy is much higher for the twisted longeron than the perfect longeron. These corroborating results suggest that a twisted longeron is more stable up to the critical buckling load than a straight longeron because the twist creates a saddle shape that prevents buckles from forming.

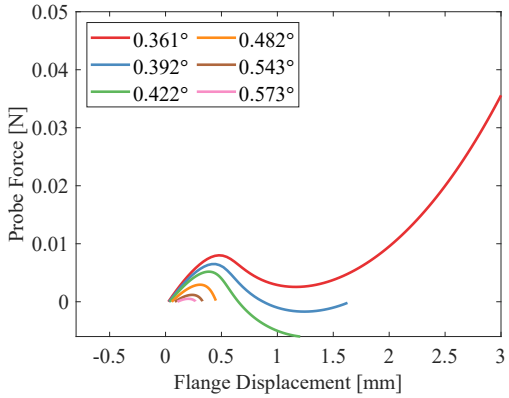

(a) Probe force vs. flange displacement, perfect longeron

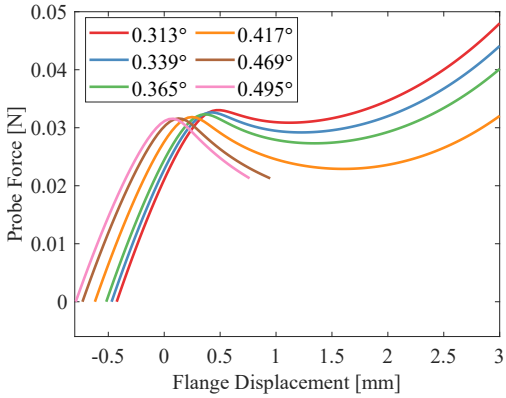

(b) Probe force vs. flange displacement, twisted longeron

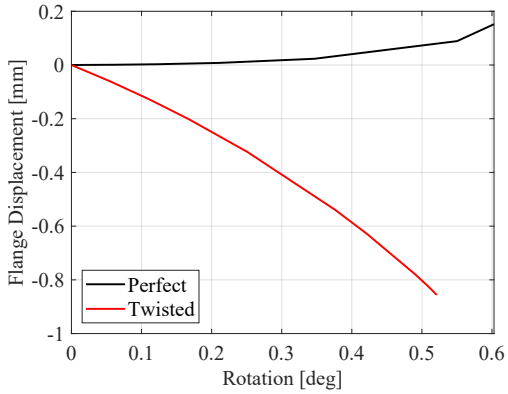

(c) Vertical displacement of flange in center of longeron

Fig. 17 (a) and (b): Comparison of probe force vs. flange displacement curves (where positive displacement is upwards) for numerical perfect and twisted longerons with $\theta = 105°$. (c): Comparison of vertical displacement of flange edge in center of longeron vs. imposed rotation during bending.

VII. Conclusion and Future Work

This work studied the effect of varying the flange subtended angle on the stability of TRAC longerons. 3D-printed and composite experimental longerons as well as perfect numerical composite longerons were studied. For all three, the critical buckling bending moment increases with increasing flange subtended angle. The critical energy at all imposed rotations also increases with increasing flange subtended angle for all three types of longerons tested. Thus, the results presented suggest that increasing the flange subtended angle of longerons increases their stability both in terms of increasing their critical buckling load and increasing their stability approaching the buckling load. An additional benefit to increasing the flange subtended angle is that it increases the longeron's stiffness, as seen for all three types of longerons tested. Therefore, increasing the flange subtended angle of longerons will enable them to support higher loads without buckling and with smaller deflections.

The similarities between the trends in the results for the 3D-printed and composite longerons show that 3D-printed thin shell structures have similar behavior to composite thin shell structures. Thus, in some cases, 3D-printed structures can be used for preliminary studies when it is desired to study multiple different designs with little manufacturing time to produce each prototype.

This work also studied the effect of twist on the stability of longerons. In comparison with a perfect straight longeron, a twisted longeron has a lower critical buckling load. On the other hand, the saddle shape created by the twist significantly increases the stability of twisted longerons approaching the critical buckling load by preventing buckles from forming and requiring a greater energy input to trigger local instability below the critical buckling load. Thus, in situations where it is important to prevent early buckling caused by imperfections or sudden loading, intentionally applying a twist to longerons, or other cylindrical structures, may be beneficial.

Future work will include experimentally testing more composite longerons with all three flange subtended angles to verify that the trends of increasing stability with subtended angle are repeatable. A study of the effects of decreasing the flange radius on the stability of composite longerons will also be performed. If the results are favorable, the flange radius will be decreased in proportion to the increase in subtended angle to keep the arc length, and thus mass, of the longerons constant.

Additionally, the effects of twist on longeron stability will be further studied, since imposing twist may be a way to increase stability without changing the longeron's cross sectional parameters. Further probing studies will be conducted on the twisted longerons to verify that the twist does not create local instabilities. Also, the full twist profile of the experimental longerons will be characterized and used in the numerical model of the twisted longeron to see if better agreement between the numerical and experimental results can be achieved. Better agreement will help confirm that the differences between the experimental and perfect numerical results are indeed mainly due to the twist in the experimental longerons.

Acknowledgments

This research was carried out with financial support from the National Science Foundation's Graduate Research Fellowship Program, the Caltech Space Solar Power Project, and the Caltech Resnick Sustainability Institute in support of the Caltech WAVE Fellows program.

References

[1] Von Karman, T., and Tsien, H. S., "The Buckling of Thin Cylindrical Shells Under Axial Compression," *Journal of the Aeronautical Sciences*, Vol. 8, No. 8, 1941, pp. 303–312. https://doi.org/10.2514/8.10722.

[2] Koiter, W. T., *On the Stability of Elastic Equilibrium*, H. J. Paris, Amsterdam, Holland, 1945, Chap. 8, pp. 201–213.

[3] Donnell, L. H., and Wan, C. C., "Effect of Imperfections on Buckling of Thin Cylinders and Columns Under Axial Compression," *Journal of Applied Mechanics*, Vol. 17, No. 1, 1950, pp. 73–83.

[4] Hunt, G. W., and Neto, E. L., "Localized Buckling in Long Axially-Loaded Cylindrical Shells," *Journal of the Mechanics and Physics of Solids*, Vol. 39, No. 7, 1991, pp. 881–894. https://doi.org/10.1016/0022-5096(91)90010-L.

[5] Thompson, J. M. T., "Advances in Shell Buckling: Theory and Experiments," *International Journal of Bifurcation and Chaos*, Vol. 25, No. 1, 2015, p. 1530001. https://doi.org/10.1142/S0218127415300013.

[6] Virot, E., Kreilos, T., Schneider, T. M., and Rubinstein, S. M., "Stability Landscape of Shell Buckling," *Physical Review Letters*, Vol. 119, 2017, p. 224101. https://doi.org/10.1103/PhysRevLett.119.224101.

[7] Marthelot, J., Jimenez, F. L., Lee, A., Hutchinson, J. W., and Reis, P. M., "Buckling of a Pressurized Hemispherical Shell Subjected to a Probing Force," *Journal of Applied Mechanics*, Vol. 84, No. 12, 2017. https://doi.org/10.1115/1.4038063.

[8] Royer, F., and Pellegrino, S., "Probing the Buckling of Thin-Shell Space Structures," Ph.D. thesis, Caltech, 2021.

[9] Arya, M., Lee, N., and Pellegrino, S., "Ultralight Structures for Space Solar Power Satellites," *AIAA Scitech Forum*, 2016.

[10] Murphey, T. W., and Banik, J., "Performance Validation of the Triangular Rollable and Collapsible Mast," *Proceedings of the 24th Annual AIAA/USU Conference on Small Satellites*, AIAA, Logan, UT, 2011.

[11] Leclerc, C., and Pellegrino, S., "Nonlinear Elastic Buckling of Ultra-Thin Coilable Booms," *International Journal of Solids and Structures*, Vol. 203, 2020, pp. 46–56. https://doi.org/10.1016/j.ijsolstr.2020.06.042.